communications materials

A Nature Portfolio journal

Article

https://doi.org/10.1038/s43246-026-01306-7

Equilibrium trions on the surface of Ta_2NiS_5

Check for updates

Yuval Nitzav[1], Abigail Dishi[1], Himanshu Lohani[1], Ittai Sidilkover[2,3], Noam Ophir[1], Roni Anna Gofman[1], Avior Almoalem[1], Ilay Mangel[1], Nitzan Ragoler[1], Francois Bertran[4], Jaime Sánchez-Barriga[5,6], Dmitry Marchenko[5], Andrei Varykhalov[5], Nicholas Clark Plumb[7], Irena Feldman[1], Hadas Soifer[2,3], Anna Keselman[1,8] & Amit Kanigel[1,8] ✉

Trions, three-body bound states composed of an exciton and an additional charge, are typically fragile and require external excitation to form. Here, we report the spontaneous emergence of stable trions at the surface of the layered semiconductor Ta_2NiS_5, revealed through angle-resolved photoemission spectroscopy. We observe a sharp, highly localized in-gap feature that cannot be explained by conventional band-theory. Instead, we argue that it arises from the formation of negative trions, stabilized by surface-induced band bending and the material's quasi-one-dimensional geometry. Unlike excitons, these trions form without optical pumping and persist at equilibrium, marking a rare example of an interaction-driven surface state in a nominally conventional semiconductor. Our findings establish Ta_2NiS_5 as a unique platform for exploring many-body physics at surfaces and open new avenues for studying and controlling collective excitations in low-dimensional systems.

Quasiparticles composed of multiple interacting particles underpin much of modern condensed matter physics. While single particle excitations, such as electrons and holes, are ubiquitous, composite bound states, such as excitons, polarons and Cooper pairs, emerge only under special conditions and can drive new phases of matter. Among the most intriguing are trions, three body bound states of two electrons and one hole (or vice versa), which are a hallmark of strong Coulomb interactions in reduced dimensions. In semiconductors and two-dimensional materials, trions are usually generated transiently by optical excitation and decay within picoseconds, making equilibrium trions in solid-state systems without continuous pumping a long-standing challenge.

Excitons govern light absorption and emission in many semiconductors and become especially prominent when quantum confinement raises their binding energy above thermal fluctuations. In doped systems or in the presence of excess carriers, an exciton can bind an additional electron or hole to form a trion, or charged exciton, producing distinct low-energy optical features[1].

Two-dimensional materials, such as transition metal dichalcogenides (TMDs) provide an ideal setting, where strong Coulomb interactions and reduced dielectric screening yield large exciton and trion binding energies, enabling direct observation in photoluminescence and absorption experiments[2,3].

Excitons and trions are rarely present under equilibrium conditions. However, in narrow-gap or semimetallic systems, strong Coulomb interactions can result in exciton binding energies (E_{ex}^{b}) that are larger than the bandgap (E_g) and lead to the spontaneous formation of excitons even in equilibrium. When these spontaneously-formed excitons condense, they can drive a phase transition into a novel collective state, giving rise to the excitonic insulator (EI) phase[4]. Dimensionality plays a crucial role in stabilizing these bound states, as it strongly influences the dielectric environment, potentially enhancing Coulomb interaction and thus enlarging the exciton binding energy[3,5,6]. Several materials have been proposed as realizations of the excitonic insulator phase, though unambiguous experimental confirmation remains limited.

An alternative route to an excitonic insulator is through carefully engineered systems. Using such devices, it is possible to manipulate the exciton properties[7], prolong their lifetimes[8], or use them as spectroscopic tools to probe other material properties[9]. Remarkably, in some engineered systems, carefully tailored environments create conditions favorable for the formation of an excitonic insulator, allowing excitons to condense spontaneously even without external excitation[10–14].

[1]Department of Physics, Technion, Haifa, Israel. [2]School of Physics and Astronomy, Faculty of Exact Sciences, Tel Aviv University, Tel-Aviv, Israel. [3]Center for Light-Matter Interaction, Tel Aviv University, Tel Aviv, Israel. [4]SOLEIL Synchrotron, L'Orme des Merisiers, Saint-Aubin, France. [5]Helmholtz-Zentrum Berlin für Materialien und Energie, Elektronenspeicherring BESSY II, Berlin, Germany. [6]IMDEA Nanoscience, C/ Faraday 9, Campus de Cantoblanco, Madrid, Spain. [7]Photon Science Division, Paul Scherrer Institute, Villigen PSI, Switzerland. [8]The Helen Diller Quantum Center, Technion, Haifa, Israel.
✉e-mail: amitk@physics.technion.ac.il

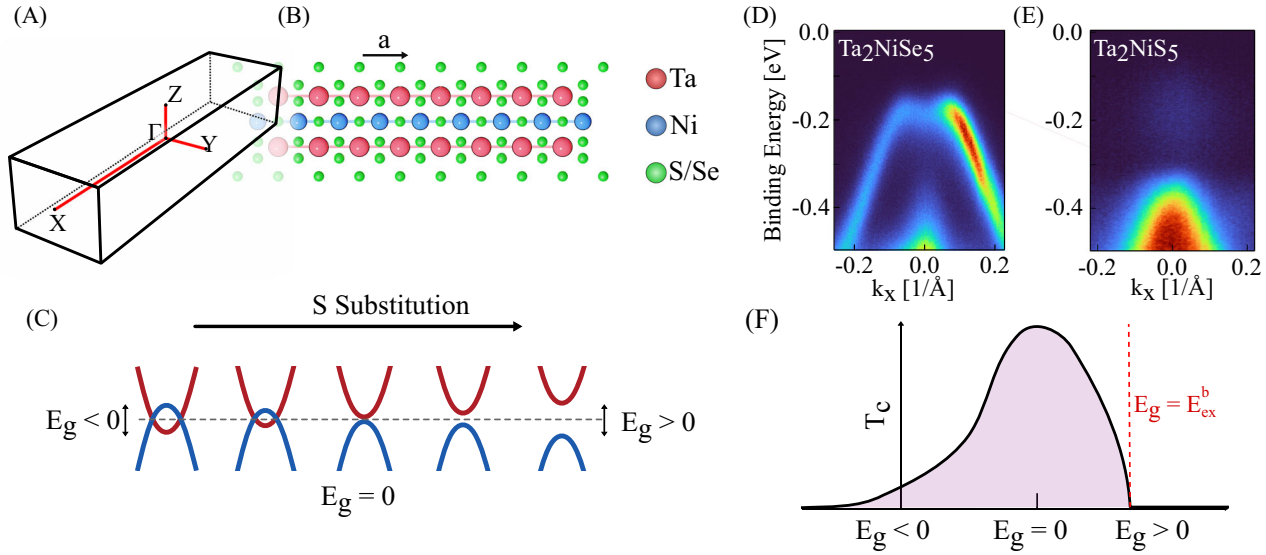

Fig. 1 | Sulfur substitution in the excitonic insulator candidate $Ta_2Ni(Se_{1-x}S_x)_5$. **A** Brillouin zone of $Ta_2Ni(Se_{1-x}S_x)_5$, with high-symmetry points indicated. The Γ--X direction corresponds to the quasi-1D chain direction shown in (**B**). **B** Simplified crystal structure of $Ta_2Ni(Se_{1-x}S_x)_5$. Each unit cell contains one Ni atom (blue) and two Ta atoms (red), coordinated by Se/S atoms. The atoms are arranged in chains along the crystallographic a-axis, giving rise to a quasi-one-dimensional structure **C** Schematic illustration of the band structure evolution in $Ta_2Ni(Se_{1-x}S_x)_5$ as sulfur gradually replaces selenium, highlighting the transition from a semimetallic to a semiconducting state. **D** ARPES image of the top of the valence band in Ta_2NiSe_5, exhibiting the characteristic "M"-shaped dispersion commonly associated with an excitonic insulator[55]. **E** ARPES image of the fully sulfur-substituted compound Ta_2NiS_5, showing a shift of the valence band to higher binding energies. A faint in-gap feature is observed at approximately 165 meV. **F** Schematic phase diagram of an excitonic insulator (adapted from ref. 4). In the semiconducting regime, increasing the band gap reduces the excitonic condensation temperature until a critical point is reached at which the exciton binding energy equals the band gap ($E_g = E_{ex}^b$), resulting in $T_c = 0$.

Trions having significant binding energies have been observed mainly in finely tuned two-dimensional systems, such as monolayer transition metal dichalcogenide[2], as well as in 1D systems like carbon-nanotubes[15–17].

One of the candidate materials proposed to host an excitonic-insulator ground state is Ta_2NiSe_5. It is a quasi-one-dimensional system composed of Ta and Ni chains running along the crystallographic a-axis, resulting in a highly anisotropic Brillouin zone (see Fig. 1A, B). There is an ongoing debate over whether Ta_2NiSe_5 is truly an excitonic insulator. While several studies present evidence supporting this scenario[18–20], with evidence from angle-resolved photoemission spectroscopy (ARPES) showing a phase transition leading to an M-shaped gap (see Fig. 1D), the structural transition that accompanies the electronic phase change complicates the interpretation of experimental observations[21].

Upon substituting sulfur for selenium, the system evolves from a semimetal into a narrow-gap semiconductor (Fig. 1C). In Fig. 1E, D, we show the ARPES images of the top of the valence band of Ta_2NiSe_5 and Ta_2NiS_5, respectively. The transition temperature decreases and eventually vanishes at a critical Se/S ratio, where $E_{ex}^b = E_g$[18,22,23] (Fig. 1F). Ta_2NiS_5, the fully substituted compound, is generally regarded as a conventional semiconductor with a direct bandgap of a few hundreds meV[23–25] presumably having $E_{ex}^b < E_g$.

However, the apparent simplicity of Ta_2NiS_5 invites further scrutiny. The strong Coulomb interactions are still present, and excitonic fluctuations could persist. In this paper, we are using ARPES to study in detail the low-energy spectral features in Ta_2NiS_5. We identify an unusual in-gap state that is sharply localized in momentum space, an observation that cannot be accounted for by conventional band structure theory. To explain this feature, we propose a theoretical model based on the formation of negative trions, which captures the key characteristics of the in-gap state. This interpretation is supported by direct measurements of the conduction band, confirming that the energetic conditions required for trion formation are met. Additional support comes from surface doping experiments, which reveal a systematic evolution of the in-gap spectral weight, consistent with a trion-based mechanism. Finally, detailed spectral function calculations within the trion framework provide a comprehensive description of the experimental data.

Results

In-gap state

We begin by examining the electronic structure of Ta_2NiS_5. Figure 2 shows ARPES spectra of Ta_2NiS_5, along the Ta-Ni chain direction (A) and perpendicular to the chains (D). The top of the valence band at the Γ point appears at a binding energy of approximately 420 meV, consistent with previous reports[23]. The effective mass of the uppermost hole-like band is about $0.3 \pm 0.04 m_e$.

Upon zooming into the energy gap region, displayed with an intensity scale 40 times larger in Fig. 2A, we observe a faint, sharply localized spectral feature centered around 165 meV below the Fermi level at the Γ point. In Fig. 2B, we show the energy distribution curve (EDC) at the Γ-point, the in-gap state remains clearly separated from the valence band, yet does not intersect the Fermi level, indicating its unusual character.

In Fig. 2C, we present the dispersion of the in-gap state along the chain direction, extracted by fitting Gaussian functions to the EDCs. We observe a hole-like dispersion confined within ± 0.2 Å^{-1} along the one-dimensional chain direction, beyond which the spectral intensity drops off sharply (see Supplementary Material (SM) for details of the fitting procedure). The bandwidth of the in-gap state is approximately 20 meV, and a parabolic fit yields an effective mass of about 3 m_e, roughly an order of magnitude larger than the effective mass of the valence band.

In Fig. 2D, we show the dispersion perpendicular to the chains' direction. The effective mass of the valence band in this direction is about three times larger than along the chains. The in-gap state appears nearly dispersionless and delocalized in momentum space. The binding energy of the in-gap state, presented in Fig. 2E at the Γ and Y points (and in between), across multiple Brillouin zones, remains constant, confirming the absence of dispersion perpendicular to the chains. Binding energies were extracted from EDC's shown in Fig. 2F. Similar behavior is observed for the dispersion

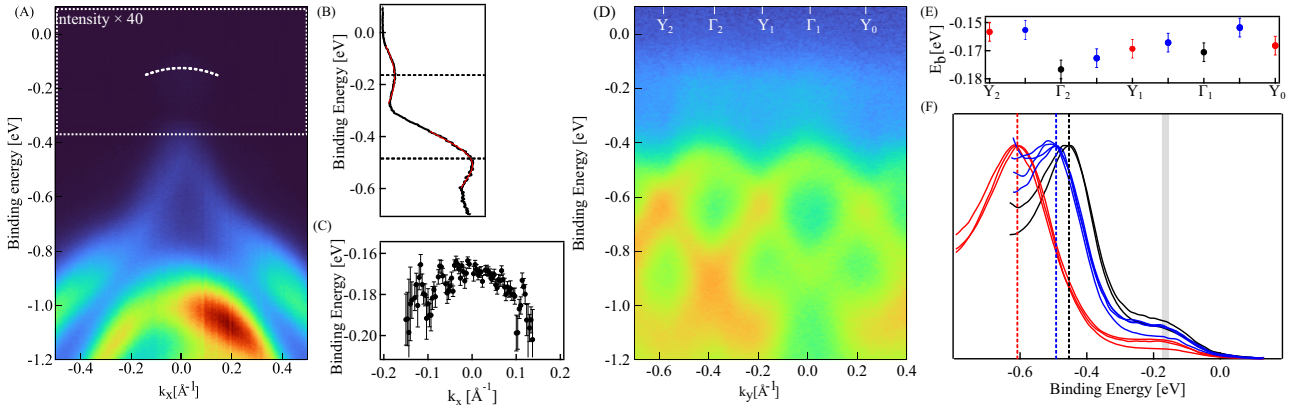

Fig. 2 | Characterization of the in-gap state in Ta_2NiS_5. A ARPES spectrum measured with 22 eV photons along the chain direction (Γ-X), revealing a faint and compact in-gap state located ~ 165 meV below the Fermi level. The intensity in the marked region (white dotted line) is enhanced by a factor of 40 for visibility. The overlaid curve shows the dispersion of the in-gap state along k_x, as extracted from (**C**). **B** Energy distribution curve (EDC) at the Γ point, clearly showing the in-gap state energetically separated from both the valence band and the Fermi level. The binding energies of the in-gap state and valence band maximum are indicated by dashed lines. **C** Dispersion of the in-gap state along k_x, extracted by fitting the EDC peaks. Points represent the best-fit peak positions ($n = 130$); error bars represent the 1 σ uncertainty from the fitting procedure. A clear hole-like dispersion is observed, with spectral weight abruptly vanishing beyond ± 0.2 Å^{-1}. Data are shown only where the fits are reliable. **D** ARPES spectrum along Γ-Y (50 eV photons, linear horizontal polarization), i.e., perpendicular to the chains. The spectrum is shown on a logarithmic scale and has been FFT-filtered for clarity. The same in-gap state is present but remains completely flat, underscoring its strong one-dimensional character. **E** Binding energy of the in-gap state measured at various momenta across multiple Brillouin zones. Points are the best-fit peak position from Gaussian fits to the EDCs ($n = 134$); error bars indicate the 1 σ fitting uncertainty. The dispersion remains flat within experimental resolution. **F** EDCs corresponding to the momentum points shown in (**E**). The valence band exhibits a clear dispersion, while the in-gap state remains fixed in energy. Dashed vertical lines mark the valence band peak positions, and the shaded gray band highlights the energy range of the in-gap state.

out-of-plane (Γ-Z) (Fig. S2 in SM (Supplementary information. See online supplementary material.)).

We noticed that the spectral weight of this anomalous in-gap state varies significantly between cleaves, sometimes prominent and well-defined, other times nearly invisible. A weak in-gap feature was in fact reported previously by Chiba et al.[26], who attributed a small spectral weight around − 0.2 eV to a surface state within the band gap. In contrast, in other ARPES studies this feature is not resolved[23], likely due to its low relative intensity and strong sensitivity to surface conditions. However, we emphasize that whenever the in-gap state is observed, its binding energy and momentum-space characteristics remain remarkably consistent, supporting its intrinsic origin.

We find that the in-gap state shows only a weak temperature dependence between 20K and room temperature (see Fig. S4 in SM (Supplementary information. See online supplementary material.) for more details).

Energetics and trion interpretation

The central question that emerges is: what is the microscopic origin of this unusual in-gap state? One possible interpretation is that the in-gap state originates from excitons, particularly given Ta_2NiS_5's proximity to the excitonic-insulator phase observed in the compound $Ta_2Ni(S_xSe_{x-1})_5$. While excitons cannot be directly probed by photoemission, ARPES can nonetheless provide insights into their presence and properties through their influence on the single-particle spectral function. In particular, theoretical frameworks have been developed to interpret excitonic signatures in time-resolved ARPES spectra[27]. A photoemission process that dissociates an exciton should produce a spectral feature located E^b_{ex} below the bottom of the conduction band, since this is the additional binding energy that must be supplied to break the exciton apart. Signatures of excitons have been provided by pump-probe ARPES experiments[28,29]. Mahan excitons that can be created in metals[30] were also measured using ARPES[31]. The characteristic "ball"-like spectral shape of our in-gap state closely resembles the excitonic fingerprint observed in time-resolved ARPES experiments in TMDs[28,32] and Topological Insulators[29]. Of particular relevance for this work is the claim of a signature of excitons at temperatures above the phase transition in Ta_2NiSe_5[33].

However, a key distinction must be noted. While Ta_2NiSe_5 is widely regarded as an excitonic insulator, Ta_2NiS_5 is not. Therefore, in Ta_2NiSe_5, the exciton binding energy, E^b_{ex}, is expected to exceed the band gap, E_g, implying that a photoemission process that dissociates an exciton should produce a spectral feature located *below* the valence band maximum. Such a feature has indeed been observed in ARPES experiments[33], although its interpretation as a signature of excitons remains a subject of ongoing debate[34]. In the case of Ta_2NiS_5 studied here, attributing the 165 meV in-gap feature to an exciton would result in $E_g > E^b_{ex}$, in agreement with it being a semiconductor, which should make thermally excited excitons very rare. The very weak temperature dependence of the in-gap state indicates that it is not governed by a thermally excited exciton population.

We propose that the in-gap feature observed in our measurements originates from trions: three-body bound states consisting of an exciton bound to an additional electron. These trions form in the presence of excess surface charge, offering a natural explanation for the observed spectral signature as we discuss below. Unlike simple excitonic models, which are incompatible with the energetics of the system, the trion scenario resolves this contradiction by invoking a more strongly bound composite state, stabilized by the extra electron-exciton interaction, E^b_{ex-e}. The total trion binding energy, $E^b_{tr} = E^b_{ex} + E^b_{ex-e}$, can then exceed the band gap even if the exciton binding energy E^b_{ex} alone does not. In such cases, individual excitons cannot form spontaneously, but the presence of an additional surface electron enables the formation of a trion.

In a photoemission process, such a trion can be broken, leaving an exciton behind. This process is illustrated in Fig. 3A. Similarly to the signature left by the disassociation of an exciton, we show below that the disassociation of a trion should produce a spectral feature located E^b_{ex-e} below the bottom of the conduction band, since this is the additional binding energy needed to break the trion into the photo-emitted electron and the leftover exciton.

To determine the exciton and trion binding energies from the ARPES spectra, it is therefore necessary to first estimate the single-particle gap: the energy difference between the bottom of the conduction band and the top of the valence band, illustrated in Fig. 1C. For this purpose, we employed two-photon photoemission (2PPE) to probe the unoccupied electronic states. In

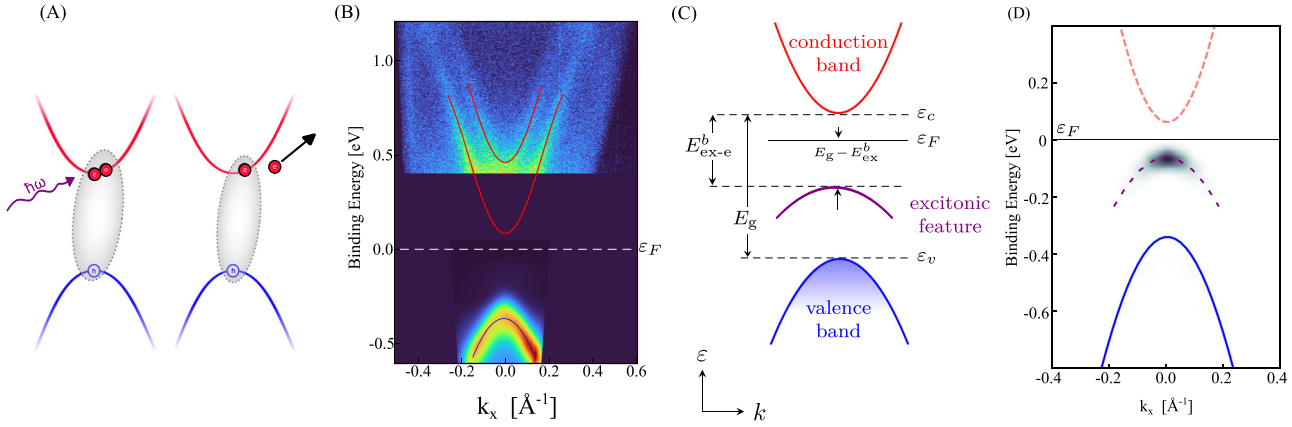

Fig. 3 | Photoemission process and energetics. A Schematic of the photoemission process involving a trion. Left: Initial ground state where an exciton and a conduction-electron form a trion bound state. Right: upon photon absorption, one electron is emitted, breaking the trion and leaving behind a neutral exciton. **B** The 6.4 eV ARPES spectra showing the top of the valence band, combined with the 6 eV 2PPE spectra showing the bottom of the conduction band. The solid lines are fits to the data using a simple model. More details about the model can be found in the SM. **C** Illustration of the band structure and the the in-gap feature resulting from the exciton remaining after breaking a trion. Conduction band (red), valence band (blue) and in-gap feature (magenta). The excitonic binding energy (E^b_{ex}) and the electron-exciton binding energy (E^b_{ex-e}) are indicated. **D** Calculated spectral function obtained in the presence of a single trion, due to photoemission of a conduction electron, obtained using exact diagonalization (ED) on the minimal model presented in the text. To mimic the finite temperature and resolution of the ARPES measurement we use convolution with a Gaussian of width 20 meV.

Fig. 3B, we show the 2PPE data combined with ARPES data, showing the single particle gap. The measurement reveals two parabolic bands. By applying a simple fitting model, we estimate that the bottom of the conduction band, ϵ_c, lies approximately 85 ± 20 meV above the Fermi level. More details are provided in the SM. The top of the valence band is found at a binding energy of 420 ± 40 meV. Yielding a band gap of about 500 ± 40 meV, comparable to previous reports[23,35].

We now turn to a more careful analysis of the energetics. In the experimental setup, the system is coupled to a charge reservoir that fixes the chemical potential. In this situation, an electron can be transferred from the reservoir into the conduction band. In a non-interacting system, this occurs when the bottom of the conduction band, ϵ_c, crosses the Fermi level, ϵ_F. However, interactions can significantly modify this condition.

In particular, the formation of a bound trion state can render charge transfer energetically favorable even when $\epsilon_c > \epsilon_F$. The key requirement is that the total binding energy of the trion, $E^b_{tr} = E^b_{ex} + E^b_{ex-e}$, exceeds the sum of the single-particle gap E_g and the energy cost $(\epsilon_c - \epsilon_F)$ of placing an electron in the conduction band. That is, charge transfer can form when:

$$E^b_{tr} \geq E_g + (\epsilon_c - \epsilon_F) \tag{1}$$

Equivalently, Eq. (1) can be viewed as a condition on the Fermi level $\epsilon_F \geq \epsilon_c + E_g - E^b_{tr}$ for the charge transfer to occur.

We note that, although the Fermi level is defined as the energy required to add a single electron to the system, in this case, its addition also induces the formation of an exciton, which subsequently binds to the added electron.

In the presence of a *single trion* (or more realisticaly - a low density of trions), a photoemission process that breaks it will result in a spectral feature at energy E^b_{ex-e} below the bottom of the conduction band or, equivalently, $E_g - E^b_{ex}$ below the Fermi level. This energy balance is illustrated in Fig. 3C.

Based on this analysis and the positions of the valence and conduction bands, as well as the position of the in-gap feature, observed experimentally we can extract the binding energies in the system, yielding $E^b_{ex} = 340 \pm 60$ meV and $E^b_{ex-e} = 250 \pm 50$ meV.

Theoretical model and spectral function calculation

To analyze the formation of trions in the system and the expected spectral function in their presence in a more quantitative manner, we study a minimal 1D lattice model for the weakly-coupled Ta_2NiS_5 chains, accounting for the geometry of the unit cell.

A schematic picture of the model is shown in the SM in Fig. S8A (Supplementary information. See online supplementary material.). We consider two chains of conduction electrons, labeled by $\alpha = 1, 2$, and a single chain of valence electrons, corresponding to the two Ta and the single Ni chains respectively. For simplicity we consider a spinless model. The Hamiltonian is given by

$$\begin{aligned} H &= H_0 + H_{int} \\ H_0 &= -t_c \sum_{\alpha,i} c^\dagger_{\alpha,i} c_{\alpha,i+1} + t_f \sum_i f^\dagger_i f_{i+1} + D \sum_i \left(n^c_i - n^f_i\right) - \mu \sum_i \left(n^c_i + n^f_i\right) \\ H_{int} &:= \sum_{\alpha,i,j} U_{ij} n^c_{\alpha,i} n^f_j + \sum_{\alpha,\beta,i,j} V^{\alpha\beta}_{ij} n^c_{\alpha,i} n^c_{\beta,j}. \end{aligned} \tag{2}$$

Here $c_{\alpha,i}$ is the annihilation operator of a conduction electron on site i on chain $\alpha = 1, 2$, f_i is the annihilation operator of a valence electron at site i, t_c (t_f) is the intra-chain hopping amplitude on the conduction (valence) chain, D determines the single particle gap $E_g = D - 2(t_f + t_c)$, μ is the chemical potential, U_{ij} is the interaction between the conduction and valence electrons, $V^{\alpha\beta}_{ij}$ is the interaction between the conduction electrons on chains α, β, $n^c_{\alpha,i}$ (n^f_i) is the respective c_α (f)-electron number operator, with $n^c_i = \sum_\alpha n^c_{\alpha,i}$ the total density of conduction electrons. Model parameters used in the simulations are $t_c = 0.78$ eV and $t_f = 1.09$ eV, for the hopping amplitudes, corresponding to the effective masses of the conduction and valence bands, respectively. c and f hybridization is forbidden in orthorhombic phase[21]. Hopping between the two conduction chains is neglected, consistent with previous studies showing Ta-Ta chain coupling to be below 0.02 eV[36–40]. In addition, we set $D = 4.14$ eV resulting in a single particle gap equal to $E_g = 0.4$ eV.

The interactions U_{ij} and $V^{\alpha\beta}_{ij}$ are modeled using a screened Coulomb potential and their explicit form is given in the SM. While interactions between the conduction (c) and valence (f) electrons enhance both exciton and trion binding energies, interactions between conduction electrons suppress the latter. Trion formation is thus energetically favorable only if the attraction of the extra electron to the exciton's hole outweighs the repulsion from its electron. Note also that we do not include interactions between the valence electrons in the model, as we will only consider states within the single-hole occupancy subspace.

To obtain the exciton and trion binding energies, we study the model using exact diagonalization (see SM for details).

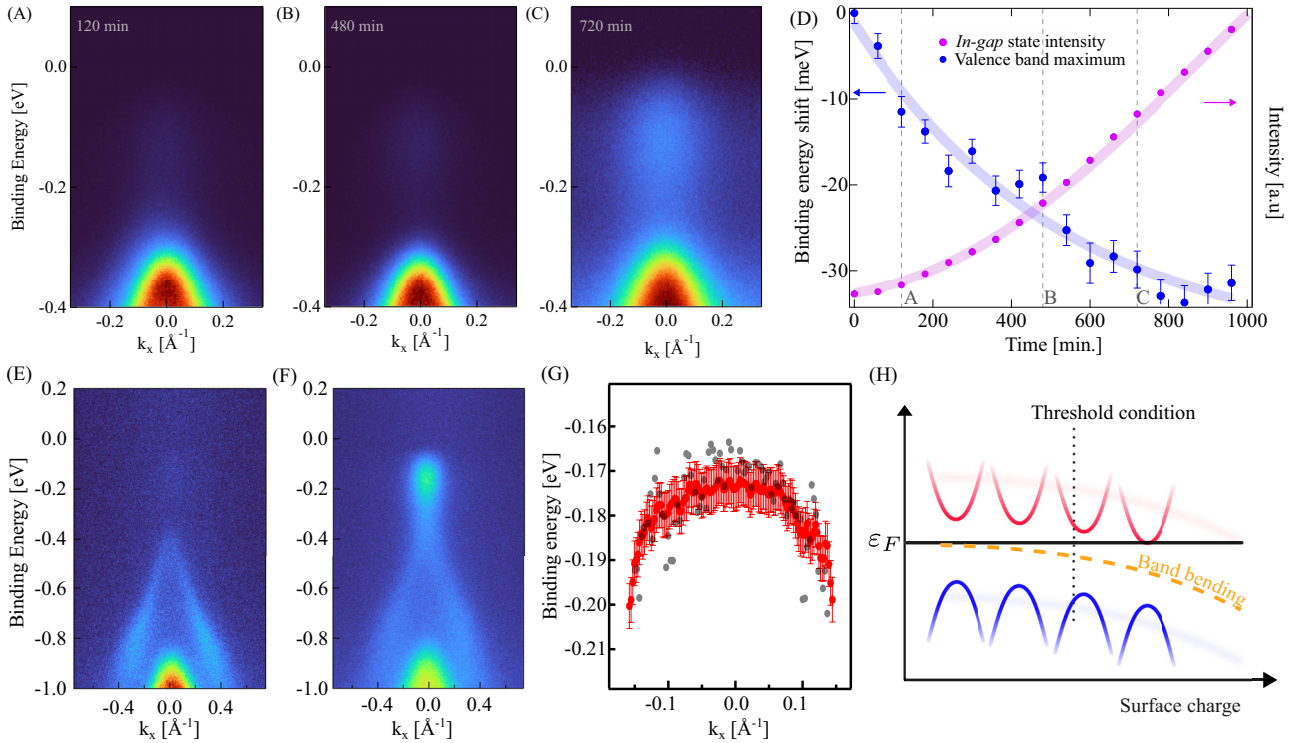

Fig. 4 | Surface doping dependence of the in-gap state. A–C ARPES spectra along the Γ-X direction measured at successive time intervals after cleaving the sample using 6.4 eV photons. **A** Two hours, no in-gap state is visible. **B** After 8 h in vacuum, a faint in-gap feature begins to emerge. **C** After 12 h, the spectral weight of the in-gap state increases significantly. **D** Time evolution of the valence band maximum (blue) and the spectral intensity of the *in-gap* state (magenta). Points for the valence band maximum are best-fit peak positions ($n = 130$), with error bars indicating the 1 σ uncertainty from the fitting procedure. Shaded lines are guides to the eye. EDCs at the Γ point as a function of time used here are shown in Fig. S6 in SM (Supplementary information. See online supplementary material.). Dashed vertical lines indicate the time points at which (**A–C**) were measured. Intensity values are normalized to the intensity of the peak of the valence band. **E–G** Controlled potassium surface doping of Ta_2NiS_5. **E, F** ARPES spectra along the Γ-X direction, taken with 43 eV photons and horizontal polarization, measured before (**E**) and after 20 s of potassium deposition (**F**). **G** Extracted dispersion of the in-gap state from (**F**) (red), overlaid with the dispersion from Fig. 2C (black) for comparison. Points represent best-fit peak positions ($n = 106$). Error bars represent the 1 σ uncertainty from the fitting procedure. **H** Schematic illustration of the effect of surface doping: band structure shifts downward, and once the condition in Eq. (1) is satisfied, trion formation becomes energetically favorable.

We find that the exciton-electron binding energy, $E^b_{\text{ex-e}}$, in the system can be significant in comparison to the exciton binding energy, with their ratio reaching a value close to one third as observed in the experiment. Specifically, for screening length $\xi = 6a$ (with $a = 3.41$ Å the unit cell length[41]), as used in the calculation of the spectral function discussed below, we obtain $E^b_{\text{ex}} \approx 0.34$ eV and $E^b_{\text{ex-e}} \approx 0.12$ eV.

We next calculate the spectral function probed by the photoemission process. Focusing on the effect of the presence of trions in the system, and assuming zero temperature, we calculate

$$A_c(k,\omega) = \sum_{\alpha}\sum_{n} |\langle\psi_n|c_{\alpha,k}|\psi_{\text{gs}}\rangle|^2 \delta\Big(\omega - (E_n - E_{\text{gs}})\Big), \qquad (3)$$

where $|\psi_{\text{gs}}\rangle$ is the many-body ground state wavefunction, E_{gs} is the ground state energy, $|\psi_n\rangle$ is the wavefunction in an excited state, and E_n is the respective energy. Here, we only consider processes in which a conduction electron is emitted from the system. We expect photoemission of valence electrons to predominantly probe the valence band and therefore forgo an explicit calculation of this process.

Assuming the density of trions is low, and to elucidate the analysis, we consider the scenario of a single trion in the ground state. A photoemission process of a conduction electron requires breaking the trion, leaving behind an electron-hole pair in the system. Thus, to obtain the spectral function, we carry out a summation over excited states $|\psi_n\rangle$ in the subspace with a single electron and a single hole. We find that the largest matrix element is with states hosting a bound exciton at momenta close to zero, resulting in the ball-like feature, as shown in Fig. 3D. Strikingly, the resulting spectrum closely matches the in-gap feature observed in our ARPES data.

Surface doping as a control knob

The density of trions is expected to depend on the level of surface doping. To investigate this dependence, we examined the evolution of the in-gap state under two conditions: (1) by allowing the sample to age in ultra-high vacuum (UHV), and (2) by depositing potassium on the surface to introduce controlled electron doping.

Figure 4A–C show ARPES spectra along the chain direction, measured with 6.4 eV photons at successive time intervals after cleaving the sample. At early times (panel A), the in-gap state is barely visible. As time progresses (panels B and C), its intensity steadily increases. Simultaneously, the valence band shifts toward higher binding energies, indicating a change in the surface potential. Previous studies have shown that such binding-energy drifts over time are related to changes in surface potential[42,43]. Panel D quantifies this evolution: the energy shift of the valence band maximum (blue) and the integrated intensity of the in-gap state (magenta) are plotted as a function of time. The growing in-gap intensity, reflecting an increasing surface trion density, tracks the downward band bending. This correlation supports our interpretation that the in-gap spectral weight is directly linked to the level of surface doping, consistent with the trion-based model.

A more controlled method for electron doping of the surface is in-situ potassium deposition on the freshly cleaved sample. In Fig. 4E, we show the ARPES spectrum acquired immediately after cleaving, where the spectral weight within the gap is very weak. Panel (F) displays the spectrum following the deposition of approximately one-tenth of a monolayer of potassium.

After deposition, we observe a slight downward shift of the valence band and a pronounced enhancement of the in-gap state intensity. Notably, the dispersion of the in-gap state post-deposition, shown in Fig. 4G, is identical to that observed in aged samples, indicating a common origin. The effect of surface doping is illustrated schematically in Fig. 4H. Doping causes a rigid downward shift of the bands. At a certain doping level, the conduction band approaches the Fermi level closely enough that Eq. (1) is satisfied, leading to the formation of the first trion.

At lower photon energies, the increased probing depth averages over surface and bulk regions with different band bending, reducing the spectral weight of the in-gap state and broadening its lineshape. This behavior is consistent with trion formation being restricted to the surface region where band bending stabilizes them.

Discussion

Let us now consider alternative origins to the in-gap state. Can the in-gap state represent the bottom of the conduction band? We argue that this interpretation is not applicable to Ta_2NiS_5, for two reasons. First, although DFT calculations for this system are challenging due to strong Coulomb interactions, there is consensus that Ta_2NiS_5 is *not* semimetallic[44], implying that the conduction band minimum lies above the Fermi level. This is in agreement with our 2PPE measurements, which directly reveal the unoccupied states. Moreover, the observed in-gap state exhibits a relatively heavy, hole-like dispersion and is never seen to cross the Fermi level, inconsistent with a conduction band origin.

Additionally, we argue that the in-gap state does not originate from an impurity band. Observing an impurity band in ARPES would require a high concentration of defects, for which we find no evidence. On the contrary, Raman spectroscopy reveals sharp phonon modes, indicating low disorder[45]. Moreover, we observe consistent spectra across samples from different growth batches, further supporting sample uniformity. Finally, the systematic evolution of the in-gap state intensity with potassium doping is inconsistent with the behavior expected from an impurity band.

How do the numbers extracted from the ARPES data using the trion model compare with existing literature? ARPES data at high temperature reveal a band gap of 415 ± 20 meV [23]. Similarly, high-temperature transport measurements report a gap of approximately 500meV[18], in agreement with our estimate. Excitonic binding energies on the order of hundreds of meV have been observed in various low-dimensional materials. For example, binding energies of approximately 240 meV have been reported in monolayers of MoS_2 and WSe_2[46], and values as high as 700 meV have been observed in monolayer WS_2[47]. In carbon nanotubes, binding energies exceeding 400 meV have been measured[48], consistent with theoretical predictions that strong one-dimensional quantum confinement leads to significantly enhanced exciton binding energies[49]. Most notably, optical measurements of Ta_2NiS_5 indicate an exciton binding energy of approximately $\alpha \cdot 160meV$ where α is of order unity[50] in agreement with our result.

The trion binding energy, E^b_{ex-e},calculated from our ARPES data to be approximately 250 meV, is relatively large but consistent with expectations for quasi-1D systems[49] with reduced screening[6]. Trion binding energies of up to 200 meV were found in carbon nanotubes[51].

The quasi-one-dimensional (quasi-1D) structure of Ta_2NiS_5 provides a natural setting for strong electronic correlations. The localization of the trion state in the out-of-chain directions, evidenced by its flat dispersion along k_y and k_z, suggests that the trion is confined primarily to individual chains. Assuming a lateral confinement width of approximately $d \sim 4$ Å, corresponding to the structural width of a single unit-cell in Ta_2NiS_5[41], the observed trion binding energy is consistent with theoretical predictions for trions in quasi-1D systems[17].

The presence of the double Ta chain, which forms the conduction band, further enhances the exciton-to-trion binding energy ratio. The negligible Ta-Ta coupling allows the two electrons in a trion to localize on different chains, increasing their average separation relative to the electron-hole distance. This reduces the Coulomb repulsion within the trion and enhances its binding energy relative to that of the exciton (see SM).

Trion-related features in ARPES have been reported in $TaSe_3$[31] and in a doped monolayer of WS_2[52]. However, the case of Ta_2NiS_5 is fundamentally different in two key respects. In those earlier systems, the bound states form in the presence of a Fermi surface, which provides a supply of low-energy carriers, essentially "cheap" particle-hole pairs, that can readily bind to the photo-hole created during the photoemission process. These are not true equilibrium trions, but transient final-state effects that manifest in the spectral function. In contrast, we argue that the in-gap state observed in Ta_2NiS_5 reflects a genuine equilibrium trion population. First, the state is clearly visible even in the absence of a Fermi surface, ruling out the possibility of photo-hole binding to ambient carriers. Second, Ta_2NiS_5 is a direct-gap semiconductor, which makes the formation of long-lived "dark" excitons, generated by one photon and detected by another, unlikely. Together, these considerations support an interpretation in which the observed in-gap feature originates from pre-existing trions in thermal equilibrium.

CONCLUSIONS

In summary, we report the discovery of a distinct *in-gap* state in Ta_2NiS_5, whose properties are incompatible with those of conventional electronic or excitonic bands. Based on a comprehensive analysis combining ARPES measurements, controlled surface doping, and theoretical modeling, we identify this feature as a trion, a three-body bound state consisting of an exciton and an additional electron. Unlike excitons, trions can remain energetically stable even when the exciton binding energy E^b_{ex} is smaller than the band gap E_g, provided that the binding energy between the exciton and the additional electron is sufficiently large. Surface doping plays a crucial role by supplying the excess electrons necessary to enable trion formation. Our results demonstrate that interaction-driven surface quasiparticles can emerge in otherwise conventional semiconductors, and establish Ta_2NiS_5 as a rare platform where spontaneous trion formation can be both stabilized and experimentally tuned.

Methods

High-quality $Ta_2NiSe_{5-x}S_x$ single crystals were synthesized via the chemical vapor transport (CVT) method. The crystallinity of samples was confirmed by XRD measurements, and the elemental composition was determined through energy-dispersive X-ray(EDX) analysis.

Photoemission experiments were performed at the ULTRA beamline at SLS (Paul Scherrer Institute, Viligen, Swizterland) and the U112-PGM and U125-PGM beamlines at BESSY-II (ARPES 1^2 and spin-ARPES setups, HZB, Berlin, Germany), and the Cassiopee beamline at Soleil (Paris, France). Samples were cleaved in situ at a base temperature of about 25 K. Given the insulating nature of the sample, particular care was taken to suppress charging, achieved by operating at low photon flux.

Potassium was deposited onto the sample surface using a calibrated getter source. Based on the getter calibration, a 20 s deposition time corresponds to 10% monolayer coverage.

Low-photon-energy data were measured in the lab at the Technion using a 6.4 eV linear horizontal polarized laser with a pulse duration of 2ps.

Two-photon photoemission (2PPE) measurements of the conductance band were performed in the lab at TAU with ultrashort (40fs) 6 eV laser pulses and linear horizontal polarization[53]. To increase the visible momentum range on the detector, a bias of −30 V was applied between the sample stage and entrance cone of the hemispherical analyzer (DA30L, Scienta)[54]. The sample was kept at 80K and at a pressure better than $1.5\ 10^{-10}$ mbar throughout the measurement. A 2PPE measurement requires a much higher intensity beam than used in equilibrium ARPES[53]. Such intensity would result in an overwhelming signal from occupied bands, and the low energy cutoff of the presented spectrum was set to avoid excessive counts.

Data availability

The data that support the findings of this study are available from the corresponding authors author upon reasonable request.

Received: 10 June 2026; Accepted: 20 July 2026;
Published online: 30 July 2026

References

1. Lampert, M. A. Mobile and immobile effective-mass-particle complexes in nonmetallic solids. *Phys. Rev. Lett.* **1**, 450 (1958).
2. Mak, K. F. et al. Tightly bound trions in monolayer mos$_2$. *Nat. Mater.* **12**, 207–211 (2013).
3. Wang, G. et al. Colloquium: excitons in atomically thin transition metal dichalcogenides. *Rev. Mod. Phys.* **90**, 021001 (2018).
4. Jérome, D., Rice, T. M. & Kohn, W. Excitonic Insulator. *Phys. Rev.* **158**, 462–475 (1967).
5. Deslippe, J. et al. Electron-hole interaction in carbon nanotubes: novel screening and exciton excitation spectra. *Nano Lett.* **9**, 1330–1334 (2009).
6. Chernikov, A. et al. Exciton binding energy and nonhydrogenic Rydberg series in monolayer WS_2. *Phys. Rev. Lett.* **113**, 076802 (2014).
7. Thureja, D. et al. Electrically tunable quantum confinement of neutral excitons. *Nature* **606**, 298–304 (2022).
8. Tang, Y., Mak, K. F. & Shan, J. Long valley lifetime of dark excitons in single-layer WSe_2. *Nat. Commun.* **10**, 4047 (2019).
9. Shimazaki, Y. et al. Strongly correlated electrons and hybrid excitons in a moiré heterostructure. *Nature* **580**, 472–477 (2020).
10. Ma, L. et al. Strongly correlated excitonic insulator in atomic double layers. *Nature* **598**, 585–589 (2021).
11. Chen, D. et al. Excitonic insulator in a heterojunction moiré superlattice. *Nat. Phys.* **18**, 1171–1176 (2022).
12. Wang, Z. et al. Evidence of high-temperature exciton condensation in two-dimensional atomic double layers. *Nature* **574**, 76–80 (2019).
13. Nguyen, P. X. et al. Perfect Coulomb drag in a dipolar excitonic insulator. *Science* **388**, 274–278 (2025).
14. Gu, J. et al. Dipolar excitonic insulator in a moiré lattice. *Nat. Phys.* **18**, 395–400 (2022).
15. Liang, S. et al. Solid state carbon nanotube device for controllable trion electroluminescence emission. *Nanoscale* **8**, 6761–6769 (2016).
16. Jakubka, F., Grimm, S. B., Zakharko, Y., Gannott, F. & Zaumseil, J. Trion Electroluminescence from semiconducting carbon nanotubes. *ACS Nano* **8**, 8477–8486 (2014).
17. Park, J. S. et al. Observation of negative and positive trions in the electrochemically carrier-doped single-walled carbon nanotubes. *J. Am. Chem. Soc.* **134**, 14461–14466 (2012).
18. Lu, Y. F. et al. Zero-gap semiconductor to excitonic insulator transition in Ta_2NiSe_5. *Nat. Commun.* **8**, 14408 (2017).
19. Wakisaka, Y. et al. Excitonic insulator state in Ta_2NiSe_5 probed by photoemission spectroscopy. *Phys. Rev. Lett.* **103**, 026402 (2009).
20. Wakisaka, Y. et al. Photoemission spectroscopy of Ta2NiSe5. *J. Supercond. Nov. Magn.* **25**, 1231–1234 (2012).
21. Watson, M. D. et al. Band hybridization at the semimetal-semiconductor transition of Ta_2NiSe_5 enabled by mirror-symmetry breaking. *Phys. Rev. Res.* **2**, 013236 (2020).
22. Volkov, P. A. et al. Failed excitonic quantum phase transition in $Ta_2Ni(Se_{1-x}S_x)_5$. *Phys. Rev. B* **104**, L241103 (2021).
23. Chen, C. et al. Anomalous excitonic phase diagram in band-gap-tuned Ta2Ni(Se,S)$_5$. *Nat. Commun.* **14**, 7512 (2023).
24. Li, L. et al. Strong in-plane anisotropies of optical and electrical response in layered dimetal chalcogenide. *ACS Nano* **11**, 10264–10272 (2017).
25. Pal, S. et al. Pressure-dependent excitonic instability and structural phase transition in Ta_2NiS_5: Raman and first-principles study. *Phys. Rev. B* **109**, 155202 (2024).
26. Chiba, Y. et al. Valence-bond insulator in proximity to excitonic instability. *Phys. Rev. B* **100**, 245129 (2019).
27. Rustagi, A. & Kemper, A. F. Photoemission signature of excitons. *Phys. Rev. B* **97**, 235310 (2018).
28. Madéo, J. et al. Directly visualizing the momentum-forbidden dark excitons and their dynamics in atomically thin semiconductors. *Science* **370**, 1199–1204 (2020).
29. Mori, R. et al. Spin-polarized spatially indirect excitons in a topological insulator. *Nature* **614**, 249–255 (2023).
30. Mahan, G. D. Excitons in degenerate semiconductors. *Phys. Rev.* **153**, 882–889 (1967).
31. Ma, J. et al. Multiple mobile excitons manifested as sidebands in quasi-one-dimensional metallic $TaSe_3$. *Nat. Mater.* **21**, 423–429 (2022).
32. Karni, O., Esin, I. & Dani, K. M. Through the lens of a momentum microscope: viewing light-induced quantum phenomena in 2D materials. *Adv. Mater.* **35**, 2204120 (2023).
33. Fukutani, K. et al. Detecting photoelectrons from spontaneously formed excitons. *Nat. Phys.* **17**, 1024–1030 (2021).
34. Chen, C. et al. Role of electron-phonon coupling in excitonic insulator candidate ta$_2$nise$_5$. *Phys. Rev. Res.* **5**, 043089 (2023).
35. Mu, K. et al. Electronic structures of layered Ta_2NiS_5 single crystals revealed by high-resolution angle-resolved photoemission spectroscopy. *J. Mater. Chem. C.* **6**, 3976–3981 (2018).
36. Mazza, G. et al. Nature of symmetry breaking at the excitonic insulator transition: Ta_2NiSe_5. *Phys. Rev. Lett.* **124**, 197601 (2020).
37. Kaneko, T., Toriyama, T., Konishi, T. & Ohta, Y. Orthorhombic-to-monoclinic phase transition of ta2nise5 induced by the Bose-Einstein condensation of excitons. *Phys. Rev. B* **87**, 035121 (2013).
38. Yamada, T., Domon, K. & Ono, Y. FFLO excitonic state in the three-chain Hubbard model for Ta_2NiSe_5. *J. Phys. Soc. Jpn.* **85**, 053703 (2016).
39. Sugimoto, K., Nishimoto, S., Kaneko, T. & Ohta, Y. Strong coupling nature of the excitonic insulator state in Ta_2NiSe_5. *Phys. Rev. Lett.* **120**, 247602 (2018).
40. Sugimoto, K. & Ohta, Y. Orbital diamagnetic susceptibility in excitonic condensation phase. *Phys. Rev. B* **94**, 085111 (2016).
41. Jain, A. et al. Commentary: the materials project: a materials genome approach to accelerating materials innovation. *APL Mater.* **1**, 011002 (2013).
42. King, P. D. C. et al. Large tunable Rashba spin splitting of a two-dimensional electron gas in Bi_2Se_3. *Phys. Rev. Lett.* **107**, 096802 (2011).
43. Bianchi, M. et al. The electronic structure of clean and adsorbate-covered Bi_2Se_3: an angle-resolved photoemission study. *Semicond. Sci. Technol.* **27**, 124001 (2012).
44. Windgätter, L. et al. Common microscopic origin of the phase transitions in Ta_2NiS_5 and the excitonic insulator candidate Ta_2NiSe_5. *npj Comput. Mater.* **7**, 210 (2021).
45. Ye, M. et al. Lattice dynamics of the excitonic insulator $Ta_2Ni(Se_{1-x}S_x)_5$. *Phys. Rev. B* **104**, 045102 (2021).
46. Park, S. et al. Direct determination of monolayer MoS_2 and WSe_2 exciton binding energies on insulating and metallic substrates. *2D Mater.* **5**, 025003 (2018).
47. Zhu, B., Chen, X. & Cui, X. Exciton binding energy of monolayer WS_2. *Sci. Rep.* **5**, 9218 (2015).
48. Maultzsch, J. et al. Exciton binding energies in carbon nanotubes from two-photon photoluminescence. *Phys. Rev. B* **72**, 241402 (2005).
49. Brown, J. W. & Spector, H. N. Exciton binding energy in a quantum-well wire. *Phys. Rev. B* **35**, 3009–3012 (1987).
50. Larkin, T. et al. Giant exciton Fano resonance in quasi-one-dimensional ta 2 nise 5. *Phys. Rev. B* **95**, 195144 (2017).
51. Möhl, C. et al. Trion-polariton formation in single-walled carbon nanotube microcavities. *ACS Photonics* **5**, 2074–2080 (2018).
52. Katoch, J. et al. Giant spin-splitting and gap renormalization driven by trions in single-layer WS_2/h-BN heterostructures. *Nat. Phys.* **14**, 355–359 (2018).
53. Sobota, J. et al. Ultrafast electron dynamics in the topological insulator Bi_2Se_3 studied by time-resolved photoemission spectroscopy. *J. Electron Spectrosc. Relat. Phenom.* **195**, 249–257 (2014).
54. Gauthier, N. et al. Expanding the momentum field of view in angle-resolved photoemission systems with hemispherical analyzers. *Rev. Sci. Instrum.* **92**, 123907 (2021).
55. Seki, K. et al. Excitonic Bose-Einstein condensation in Ta_2NiSe_5 above room temperature. *Phys. Rev. B* **90**, 155116 (2014).

Acknowledgements
We acknowledge the Paul Scherrer Institute, Villigen, Switzerland for provision of synchrotron radiation beamtime at beamline SIS of the SLS. We thank the Helmholtz Zentrum Berlin for the allocation of synchrotron radiation beamtime. We acknowledge SOLEIL for provision of synchrotron radiation facilities.

Author contributions
Y.N. and A.K. conceived the project. Y.N. performed ARPES measurements and analyzed ARPES data. I.F. synthesized the single crystals. A.D., H.L., R.A.G., A.A., I.M., I.S., and N.R acquired ARPES data. A.D. and H.L. analyzed ARPES data. F.B., J.S.B., D.M., A.V., and N.C.P. provided support at the synchrotron beam-lines. I.S. performed 2PPE measurements under the supervision of H.S. N.O. performed theoretical modeling under the supervision of A.K. Y.N., A.K., and A.K. wrote the manuscript with contributions from all authors.

Funding
A.K. discloses support from the Israel Science Foundation (Grant No. 2443/22).

Competing interests
The authors declare no competing interests.

Additional information
Supplementary information The online version contains supplementary material available at https://doi.org/10.1038/s43246-026-01306-7.

Correspondence and requests for materials should be addressed to Amit Kanigel.

Peer review information *Communications Materials* thanks the anonymous reviewers for their contribution to the peer review of this work. A peer review file is available.

Reprints and permissions information is available at http://www.nature.com/reprints

Publisher's note Springer Nature remains neutral with regard to jurisdictional claims in published maps and institutional affiliations.

Open Access This article is licensed under a Creative Commons Attribution-NonCommercial-NoDerivatives 4.0 International License, which permits any non-commercial use, sharing, distribution and reproduction in any medium or format, as long as you give appropriate credit to the original author(s) and the source, provide a link to the Creative Commons licence, and indicate if you modified the licensed material. You do not have permission under this licence to share adapted material derived from this article or parts of it. The images or other third party material in this article are included in the article's Creative Commons licence, unless indicated otherwise in a credit line to the material. If material is not included in the article's Creative Commons licence and your intended use is not permitted by statutory regulation or exceeds the permitted use, you will need to obtain permission directly from the copyright holder. To view a copy of this licence, visit http://creativecommons.org/licenses/by-nc-nd/4.0/.

© The Author(s) 2026